^{15}N NMR Relaxation Studies of Calcium-Loaded Parvalbumin Show Tight Dynamics Compared to Those of Other EF-Hand Proteins†

Christophe Baldellon,‡ Jean-René Alattia,§ Marie-Paule Strub,‡ Thomas Pauls,|| Martin W. Berchtold,⊥ Adrien Cavé,‡ and André Padilla*,‡

Centre de Biochimie Structurale, Faculté de Pharmacie, CNRS UMR 9955-INSERM U414, 15, avenue Charles Flahault, 34060 Montpellier, France, Institut d'Histologie, Université de Fribourg, Perolles, CH-1700 Fribourg, Switzerland, Department of Molecular Cell Biology, Institute of Molecular Biology, University of Copenhagen, Oster Farimagsgade 2A, DK-1353 Copenhagen, Denmark, and Division of Molecular and Structural Biology, Ontario Cancer Institute, and Department of Medical Biophysics, University of Toronto, 610 University Avenue, Toronto, Ontario M5G 2MG, Canada

Received February 10, 1998; Revised Manuscript Received April 22, 1998

ABSTRACT: Dynamics of the rat α-parvalbumin calcium-loaded form have been determined by measurement of ^{15}N nuclear relaxation using proton-detected heteronuclear NMR spectroscopy. The relaxation data were analyzed using spectral density functions and the Lipari−Szabo formalism. The major dynamic features for the rat α-parvalbumin calcium-loaded form are (1) the extreme rigidity of the helix−loop−helix EF-hand motifs and the linker segment connecting them, (2) the N and C termini of the protein being restricted in their mobility, (3) a conformational exchange occurring at the kink of helix D, and (4) the residue at relative position 2 in the Ca^{2+}-binding sites having an enhanced mobility. Comparison of the Ca^{2+}-binding EF-hand domains of α-parvalbumin−Ca^{2+}, calbindin−Ca^{2+}, and calmodulin−Ca^{2+} shows that parvalbumin is probably the most rigid of the EF-hand proteins. It also illustrates the dynamical properties which are conserved in the EF-hand domains from different members of this superfamily: (1) a tendency toward higher mobility of NH vectors at relative position 2 in the Ca^{2+}-binding loop, (2) a restricted mobility for the other residues in the binding loop, and (3) an overall rigidity for the helices of EF-hand motifs. The differences in mobility between parvalbumin and the two EF-hand proteins occur mainly at the linker connecting the pair of EF hands and also at the C terminus of the last helix. In parvalbumin−Ca^{2+}, these two regions are characterized by a pronounced rigidity compared to the corresponding more mobile regions in calbindin−Ca^{2+} and calmodulin−Ca^{2+}.

The internal dynamics of proteins may be very important for their biological function as has been shown in protein folding, enzyme catalysis, and protein−ligand interactions. Many functional aspects can be interpreted from static structures, but the extra dimension conferred by internal motions is necessary to understand how proteins function (*1*). Heteronuclear NMR relaxation techniques have emerged as a powerful approach for studying internal motions of proteins because they offer the advantage of probing individual residues throughout the molecule on a time scale that ranges from picoseconds to milliseconds. Motional properties of the NH bond vectors may be investigated by analysis of the relaxation behavior of the ^{15}N nuclei (*2*−*14*).

Parvalbumins are members of the Ca^{2+}-binding protein super family that includes calmodulin, troponin C, oncomodulin, and calbindin (*15*−*17*). All members of this family contain at least one pair of the Ca^{2+}-binding structural motifs composed of a helix−loop−helix structure, also called "EF-hand", which can bind divalent cations (*18*). Parvalbumin, calmodulin, troponin C, and calbindin D_{9K} have evolved from a common four-Ca^{2+}-binding domain protein (*15*). Calmodulin and troponin C behave as calcium sensors and interact with other proteins in a Ca^{2+}-dependent manner (*19*). In contrast, parvalbumin and calbindin are not involved in regulation processes and behave as Ca^{2+} buffers (*20*) in fast twitch muscles and fast-firing neurones. During evolution, these two proteins have lost one and two EF-hand domains, respectively. In parvalbumin, the N-terminal EF-hand domain has been deleted and the three remaining domains are called AB, CD, and EF by referring to the six α-helices of the protein structure (Figure 1). The AB domain has lost the ability to bind Ca^{2+} ions and forms a "flap structure" on top of an internal salt bridge between residues Glu-81 and Arg-75. This invariant salt bridge contributes to the stability of the parvalbumin fold (*18*). Ca^{2+} binding occurs in the CD and EF domains. Both sites are symmetrically arranged and related through short β-strands connecting the two Ca^{2+}-binding loops. Parvalbumins display a nearly spherical shape in which the six helices (A−F, see Figure 1) enclose a compact hydrophobic core constituted by side chains of aromatic and aliphatic residues. Parvalbumins are small (12

† M.W.B. is endebted to the Danish and Swiss fundations for financial support.

* Corresponding author. Telephone: 33 4 67 04 34 33. Fax: 33 4 67 52 96 23.

‡ CNRS UMR 9955-INSERM U414.

§ University of Toronto.

|| Université de Fribourg.

⊥ University of Copenhagen.

S0006-2960(98)00334-1 CCC: $15.00 © 1998 American Chemical Society
Published on Web 06/19/1998

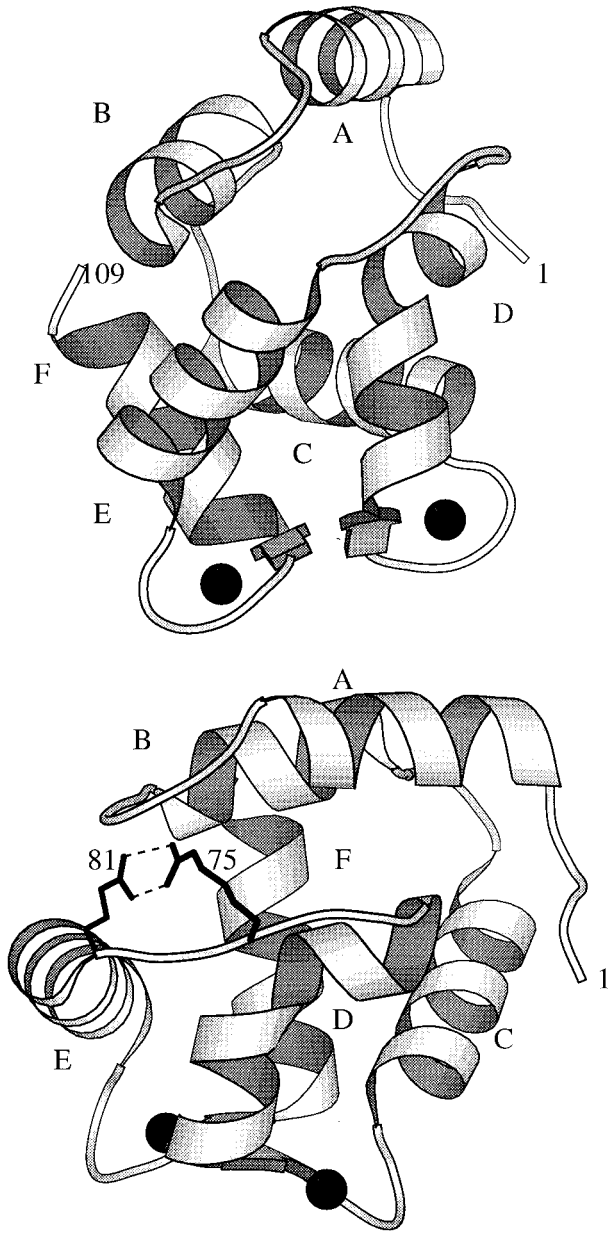

FIGURE 1: Views of the X-ray three-dimensional structure of the calcium-loaded rat α-parvalbumin first molecule (*28*). The helices are labeled A−F. The segments of the calcium-binding loops involved in the antiparallel β-type interaction are represented as broad arrows and the two calcium ions as black spheres. The salt bridge between Arg-75 and Glu-81 is shown. This figure was generated using the program Molscript (*74*).

kDa) and acidic proteins ($4 < pI < 5$). They have a remarkable thermal stability in the Ca^{2+}-loaded form as shown for example by rat parvalbumin (*21*).

From a structural point of view, parvalbumins have been studied extensively by NMR spectroscopy (*22*−*24*) and by X-ray crystallographic techniques (*18*, *25*−*28*). Comparisons between X-ray and NMR structures of the Ca^{2+}-loaded pike parvalbumin show that details of the structure are conserved between crystal and solution states. The differences mainly involve the N- and C-terminal domains, and the orientation of external side chains. The N-terminal domain is not well-defined in the X-ray structure, and the external positioning of the F helix is explained by intermolecular interactions, due to crystal packing effects. NMR studies using ^{13}C relaxation have shown that the parvalbumin structure is relatively rigid, with more mobile regions at the N and C termini (*29*).

This work includes the assignment of amide ^{15}N and proton N^1H resonances and an investigation of the extent of rapid backbone motions in the rat α-parvalbumin calcium-loaded form by measuring ^{15}N relaxation at two different spectrometer frequencies. The availability of the crystal structure of the same protein at 2.0 Å resolution (*28*) allowed us to analyze the dynamical parameters obtained from relaxation data on a structural basis. A comparison with other members of the EF-hand Ca^{2+}-binding protein superfamily like calbindin $D_{9k}-Ca^{2+}$ (*6*) and calmodulin$-Ca^{2+}$ (*30*) emphasizes several similarities and differences in the dynamical behaviors of the EF-hand calcium-binding motifs.

MATERIALS AND METHODS

Sample Preparation. Uniformly ^{15}N-labeled recombinant rat α-parvalbumin was expressed in *Escherichia coli* strain JM109 (DE3) transformed with the pGEMEX vector (Promega) containing the rat parvalbumin gene (*31*) and grown in M9 minimal media (*32*) supplemented with ampicillin (0.1 mg/mL) and using $^{15}NH_4Cl$ as the sole source of nitrogen. The protein was purified following the procedure previously described by Pauls et al. (*31*). The protein sample was dissolved in 450 μL of a 95% ^1H_2O/5% ^2H_2O mixture (v/v) to a final concentration of 4.5 mM and buffered with 50 mM sodium phosphate at pH 5.8. NMR tubes and vessels were washed with diluted HCl so paramagnetic impurities could be avoided. The ^1H NMR one-dimensional (1D) spectrum of our sample is similar to the one previously published by Pauls et al. (*31*) for the Ca^{2+}-saturated form of recombinant rat parvalbumin.

NMR Spectroscopy. All NMR spectra were recorded at 305 K on a Bruker AMX400 (9.40 T) or a Bruker AMX600 (14.10 T) spectrometer, both equipped with a three-channel interface, a pulsed field gradient probe, and a gradient amplifier unit.

Sequential assignments of ^{15}N resonances in Ca^{2+}-loaded rat α-parvalbumin are based on several types of two- and three-dimensional $^1H-^{15}N$ correlation spectra listed in Table 1 in addition to $^1H-^1H$ NOESY[1] and TOCSY data.

Measurements of ^{15}N R_1 values, ^{15}N R_2 values, and steady-state $^1H-^{15}N$ NOE values (Table 1) were taken using previously described sequences (*30*, *33*) which have been modified by introduction of pulsed field gradient purges. This suppresses the intense water signal and permits the study of amide protons in exchange with the solvent. The steady-state $^1H-^{15}N$ NOE(η) values are obtained by recording spectra with and without a proton saturation period of 3 s.

Relaxation Data Processing and Analysis. The Aurelia package (Bruker) (*34*) was used to measure 2D peak intensities (peak height). All calculations were carried out using the MATLAB package (The MathWorks, Inc.). For each peak, the error was estimated by measuring the amount of noise on the baseline taken at cross sections passing

[1] Abbreviations: 2D and 3D, two- and three-dimensional, respectively; HSQC, heteronuclear single-quantum correlation; TOCSY, total correlation spectroscopy; NOESY, nuclear Overhauser effect spectroscopy; R_1, longitudinal relaxation rate; R_2, transverse relaxation rate; CSA, chemical shift anisotropy; B_0, static main field; 1SD, one standard deviation.

Table 1: Two- and Three-Dimensional $^1H-^{15}N$ NMR Experiments and Experimental Parameters

experiment	^1H (MHz)	scan	mixing[a] and delays	recycling delay (s)	acquisition[b]	processing[b,c]	reference
$^1H-^{15}N$ HSQC	600	8		0.8	2048 × 300	2048 × 1024	*64*−*67*
3D TOCSY−HSQC	400	16	60 ms	0.8	1024 × 100 × 128	1024 × 256 × 512[d]	*47*, *64*−*67*
3D NOESY−HSQC	600	16	150 ms	0.8	1024 × 100 × 128	1024 × 256 × 512[d]	*47*, *64*−*68*
3D HSQC−NOESY−HSQC	400	16	150 ms	0.8	1024 × 100 × 128	1024 × 256 × 512[d]	*33*, *49*, *64*, *67*
T1	400	16	*e*	3	1024 × 180	2048 × 1024	*30*, *33*
T1	600	16	*e*	3	1024 × 180	2048 × 1024	*30*, *33*
T2	400	16	*f*	2.5	1024 × 180	2048 × 1024	*30*, *33*
T2	600	16	*g*	2.5	1024 × 180	2048 × 1024	*30*, *33*
$^1H-^{15}N$ NOE	400	32	3 s[h]	5	1024 × 225	2048 × 1024	*30*, *33*
$^1H-^{15}N$ NOE	600	32	3 s[h]	5	1024 × 225	2048 × 1024	*30*, *33*

[a] NOESY and TOCSY mixing times. [b] Acquisition (complex) and processed (real) size with $t_2 \times t_1$ and $F_2 \times F_1$ for 2D spectra and $t_3 \times t_2 \times t_1$ and $F_3 \times F_2 \times F_1$ for 3D spectra. Spectral width (^1H) = 5000 Hz and (^{15}N) 1400 Hz at 400 MHz. Spectral width (^1H) = 7246.4 Hz and (^{15}N) 2100 Hz at 600 MHz. Quadrature in indirect dimensions was accomplished using the States−TPPI method (*47*). GARP decoupling (*69*) was used during acquisition to decouple ^{15}N. [c] All spectra were processed on a Silicon Graphics Indigo XS24 worksation using Uxnmr or Xwinnmr software (Bruker). Sine-bell windows with $\pi/3$ and $\pi/8$ shifts were applied in ^{15}N and ^1H dimensions, respectively. All spectra were further processed using polynomial baseline corrections. [d] Linear prediction. [e] Values of 12, 52, 102, 152, 202, 302, 402, 502, 802, 2002, and 3002 ms. [f] Values of 7, 14, 32, 47, 65, 79, 112, 202, 349, 500, and 799 ms. [g] Values of 7, 14, 32, 47, 65, 79, 112, 202, 277, 349, 425, 500, and 799 ms. CPMG sequence (*70*, *71*) with the interval between ^{15}N 180° pulses set at 900 μs. Additional ^1H 180° pulses were applied every 4 ms in the CPMG pulse train to suppress cross-correlation acting on ^{15}N transverse relaxation (*72*). [h] Proton saturation period using 120° pulses applied every 5 ms (*73*).

through the maximum intensity. R_1 and R_2 values and the steady-state $^1H-^{15}N$ NOE η values were determined according to the procedure described by Alattia et al. (*29*). Briefly, values of R_1 and R_2 were determined by fitting the measured peak intensity to a single-exponential decay curve. Uncertainties in the relaxation rates were determined from Monte Carlo simulations (*35*, *36*). Values of steady-state $^1H-^{15}N$ NOE η were established from the ratio of peak intensities in spectra recorded with and without ^1H saturation. Values of the spectral density function were obtained by fitting relaxation data recorded at two spectrometer fields and using the reduced spectral density mapping (*12*, *13*, *37*−*39*). This method assumes that the high-frequency spectral density terms are approximately equal in magnitude, i.e., $J(\omega_H \pm \omega_N) \approx J(\omega_H)$, and therefore may be replaced by a single value, $J^*(\omega_H)$. This method is well-established and also appears to introduce less error in the determination of the spectral density at high frequencies than the full spectral mapping procedure initially used by Peng and Wagner (*33*, *37*) which needs additional relaxation measurements. The acquisition of two sets of data recorded at two spectrometer frequencies allows better accuracy in the determination of the spectral density function (*13*, *40*). The set of calculated $J(\omega)$ values is informative for the shape of the spectral density functions which can be in turn analyzed in terms of motion of the NH vectors. The determination of the spectral density function at zero frequency $J(0)$ can be complicated by conformational exchange, in the millisecond to microsecond time scale which contributes to the transverse relaxation rate R_2 and therefore to $J(0)$ so that $J(0)_{eff} = J(0) + \lambda R_{ex}$. The presence of a conformational exchange can therefore enhance anomalies for the R_2 and $J(0)$ values. R_{ex} is frequency-dependent and has been determined from relaxation data recorded at the two spectrometer fields (*12*, *13*).

In the presence of fast protein motions, the $J(0)$ value has an upper limit given by $2\tau_m/5$ with τ_m being the overall correlation time for an isotropic Brownian motion of the $^{15}N-^1H$ bond vector. The shape of the spectral density functions $J(\omega)$ is determined by NH bond motions. As the area under $J(\omega)$ is constant (*41*, *42*) and similar for all NH vectors, fast internal motions tend to increase $J(\omega)$ at high frequencies and therefore decrease $J(\omega)$ at low frequencies. The relative evolution of $J(\omega)$ between zero and the highest observable frequency is also dependent on the time scale of the fast motion (*38*). $J(0)$ is apparently the most sensitive probe for dynamic heterogeneity along the protein backbone. Inspection of $J(0)$ and $J^*(\omega_H)$ versus sequence provides a rapid overview of the relative mobility along the protein backbone and identifies both fast and slow dynamic processes in the protein.

The analysis by spectral density mapping is attractive because few assumptions are required about the form of either the motion of the protein or the spectral density function itself. One consequence of the fact that no model of the protein dynamics is required is that the spectral density values obtained do not provide a clear picture of the internal motions present in the protein. An alternative approach is to use explicit definitions for the form of spectral density function such as the "model-free" density function of Lipari and Szabo (*43*, *44*). In this model, assuming that the overall and internal motions contribute independently to the reorientational correlation function of $^{15}N-^1H$ vectors and that the internal motion occurs on a much faster time scale than the global rotation of the molecule, $J(\omega)$ can be expressed using the well-known expression of Lipari and Szabo (*43*) for a spherical molecule with isotropic rotational diffusion:

$$J(\omega) = S^2\tau_m/(1 + \omega^2\tau_m^2) + (1 - S^2)\tau/(1 + \omega^2\tau^2)$$
$$\text{with } 1/\tau = 1/\tau_m + 1/\tau_e$$

S^2 is the order parameter and describes the relative amplitude of the internal motions contributing to the relaxation. It ranges from 0 to 1. τ_e is the effective correlation time for rapid internal motions and τ_m the overall correlation time. An extended form of the model-free spectral density function has been developed by Clore et al. (*3*, *45*) to describe internal motions that take place on two distinct time scales, differing by at least 1 order of magnitude. An exchange term, R_{ex}, is also required to account for chemical and conformational exchange processes which affect transverse relaxation times as previously noted. The exchange rate R_{ex} is frequency-

Table 2: Spectral Density Models and Parameters Used for the Relaxation Data Analysis According to the Lipari−Szabo Formalism[a]

model	spectral density functions $J(\omega)$	optimized parameters	fixed parameters
I	$J(\omega) = {}^2/_5 S^2\tau_m/(1+\omega^2\tau_m{}^2)$	S^2	τ_m, $\tau_e = 0$
II[b]	$J(\omega) = {}^2/_5 S^2\tau_m/(1+\omega^2\tau_m{}^2) + (1-S^2)\tau_i/(1+\omega^2\tau_i{}^2)$; $\tau_i = \tau_m\tau_e/(\tau_m+\tau_e)$	S^2, τ_e	τ_m
III	$J(\omega) = {}^2/_5 S^2\tau_m/(1+\omega^2\tau_m{}^2)$; $R_2(\text{obs}) = R_2 + R_{ex}$	S^2, R_{ex}	τ_m, $\tau_e = 0$
IV	$J(\omega) = {}^2/_5 S^2\tau_m/(1+\omega^2\tau_m{}^2) + (1-S^2)\tau_i/(1+\omega^2\tau_i{}^2)$; $\tau_i = \tau_m\tau_e/(\tau_m+\tau_e)$; $R_2(\text{obs}) = R_2 + R_{ex}$	S^2, τ_e, R_{ex}	τ_m
V[c]	$J(\omega) = {}^2/_5 S_f{}^2 S_s{}^2\tau_m/(1+\omega^2\tau_m{}^2) + S_f{}^2(1-S_s{}^2)\tau_s'/(1+\omega^2\tau_s'{}^2)$; $\tau_s' = \tau_m\tau_s/(\tau_m+\tau_s)$	$S_f{}^2$, $S_s{}^2$, τ_s	τ_m, $\tau_f < 20$ ps

[a] R_2(obs) corresponds to the experimental transverse relaxation measurements and R_2 the relaxation contribution from dipole−dipole and chemical shift anisotropy. [b] From refs *43* and *44*. [c] From refs *3* and *45*.

dependent according to the relationship $R_{ex}^{600}/R_{ex}^{400} = (\omega_H^{600}/\omega_H^{400})^2 = 2.25$. A constant ratio of 2.25 is therefore expected between exchange rates measured at 600 and 400 MHz.

In the Lipari−Szabo approach, the relaxation data and steady state NOE were systematically fitted to a set of five motional models as listed in Table 2 according to a procedure previously described (*46*) using nonlinear least-squares optimization and Monte Carlo error analysis (*35*, *36*). Initially, selection of the appropriate spectral density function using two time scales (model V) was not considered. The four remaining spectral density functions were considered appropriate if they satisfy two conditions. (1) The relaxation parameters R_1^{400}, R_1^{600}, R_2^{400}, and R_2^{600} and the NOE parameters η^{400} and η^{600} must be fitted within 95 and 90% confidence limits, respectively. (2) Each of the fitting parameters in the spectral density must exceed its calculated error. If more than one of the spectral density function models satisfied both conditions, then the model with the lowest χ^2 was selected. If the single-time scale spectral density functions failed to satisfy both of the above conditions, then the two-time scale model (model V) was considered and had to satisfy both conditions 1 and 2 to be retained.

Prior to selection of the most appropriate model, the correlation time τ_m was determined by minimizing χ^2, simultaneously from R_1, R_2, and ^{1}H−^{15}N NOE η data at 400 and 600 MHz, while excluding residues with an R_2/R_1 ratio outside ±1SD from the average value (*3*).

RESULTS

Assignment of Amide ^{15}N Resonances

Beginning with preliminary assignments of proton resonances obtained from NOESY and TOCSY spectra, the sequential assignments of ^{15}N resonances for Ca^{2+}-loaded rat α-parvalbumin were determined using 2D ^{1}H−^{15}N HSQC, 3D ^{1}H−^{15}N NOESY−HSQC, and 3D ^{1}H−^{15}N TOCSY−HSQC heteronuclear spectra (*47*, *48*). To confirm and complete the assignments, a 3D ^{1}H−^{15}N HSQC−NOESY−HSQC experiment was performed which more fully exploited the ^{15}N chemical shift dispersion to resolve overlapping peaks (*49*, *50*). An example of a sequential walk from residue Glu-81 to residue Glu-100 is shown in Figure 2. A total of 107 out of 109 backbone amide ^{15}N resonances were assigned, and the corresponding ^{15}N and ^{1}H chemical shifts are available as Supporting Information. The cross-peaks corresponding to residues 1 and 2 could not be observed in this analysis.

Measured Relaxation Parameters

The values of the relaxation parameters R_1, R_2, and ^{1}H−^{15}N NOE at 400 MHz (9.40 T) and 600 MHz (14.10 T) are shown in Figure 3. ^{15}N relaxation data have been obtained for 105 residues at 400 MHz, with the exception of Ala-1, Met-2, Asp-79, and Asp-76, and for 106 residues at 600 MHz, with the exception of Ala-1, Met-2, and Asp-79. The average R_1 value is 2.61 ± 0.14 s^{-1} at 9.40 T and 1.57 ± 0.07 s^{-1} at 14.10 T. The R_1 values display small variations along the sequence with minima mainly occurring between helices. The average R_2 value increases from 8.93 ± 0.57 s^{-1} at 9.40 T to 10.18 ± 0.80 s^{-1} at 14.10 T, and the corresponding R_2 profiles exhibit a similar behavior along the sequence with a small decrease in the AB and BC loops. The R_2 profiles are essentially uniform in Ca^{2+}-binding domains CD and EF with a few exceptions. Ile-66 displays the maximum value for R_2. In contrast, Lys-91 and Ser-109 display minimal R_2 values. A similar low R_2 value is also observed for residue Thr-3 present in the N-terminal part of the sequence. The average ^{1}H−^{15}N NOE is similar at 9.40 and 14.10 T, with η values of −0.27 ± 0.04 and −0.24 ± 0.04, respectively. The analysis of ^{1}H−^{15}N NOE profiles shows low η values again associated with the AB and BC loops, and the lowest values are observed for residues Asp-22, Lys-37, and Ser-109. The N$^\epsilon$H group of the Arg-75 side chain gives relaxation values quite similar to those previously described for the backbone NH with R_1 = 2.28 s^{-1}, R_2 = 7.86 s^{-1}, and η(NOE) = −0.26 and R_1 = 1.24 s^{-1}, R_2 = 7.52 s^{-1}, and η(NOE) = −0.29, values recorded at 9.40 and 14.10 T, respectively.

Mapping of the Spectral Density Function J(ω)

The ^{15}N relaxation rate constants at a given field strength can be converted into three spectral density values, namely $J(0)$, $J(\omega_N)$, and $J(\omega_H + \omega_N)$. Relaxation measurements at the two proton frequencies of 400 and 600 MHz allow the evaluation of the $J(\omega)$ function for each NH bond at several ω values, including 0, 40, 60, 360, and 540 MHz. As expected, an initial R_2/R_1 ratio analysis indicates residues which undergo significant motions on the microsecond to millisecond time scale (*2*). Only residue Ile-66 systematically displays high R_2 values (Figure 3B,E) departing from other values in helix D. The increase of R_2 measured for this residue by reference to neighboring residues (i.e., increase of 2.3 ± 0.5 s^{-1} at 400 MHz and 4.8 ± 0.7 s^{-1} at 600 MHz) gives a ratio, as expected, close to the one of the squared spectrometer frequencies (see Materials and Methods). An exchange term R_{ex} is therefore introduced in the fitting procedure (*12*, *13*), leading a calculated R_{ex} value for this residue of 2.16 ± 0.09 s^{-1} at 400 MHz (4.86 ± 0.09 s^{-1} at 600 MHz).

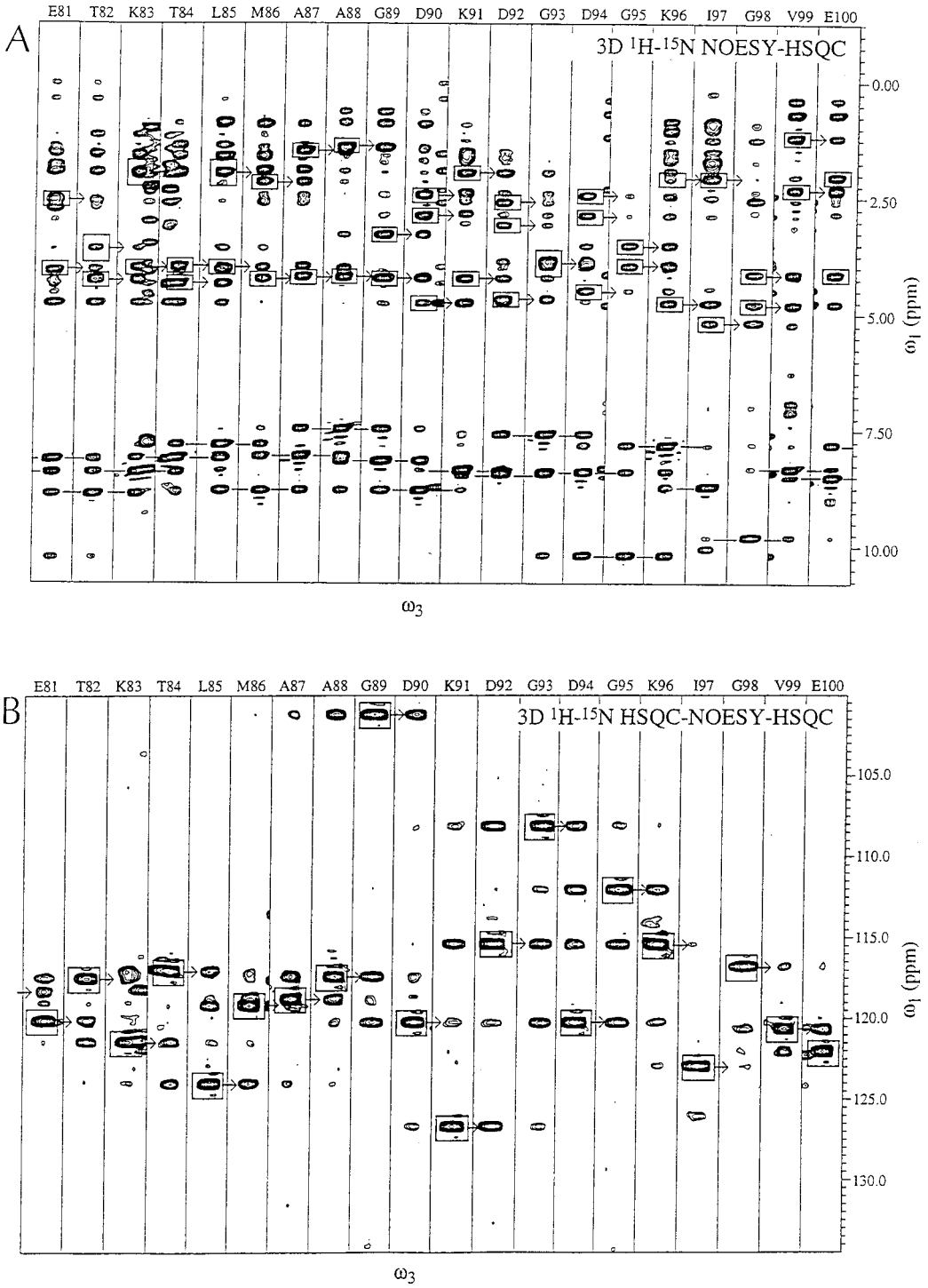

FIGURE 2: Selected ω_1 and ω_3 slices taken from 3D ^{1}H−^{15}N NOESY−HSQC (A) and 3D ^{1}H−^{15}N HSQC−NOESY−HSQC (B) spectra from residue Glu-81 to residue Glu-100 of Ca^{2+}-loaded rat α-parvalbumin at 305 K and pH 5.8. Slices are taken at ^{15}N frequencies corresponding to the residue indicated on the top of each panel. The center of each slice is located at the frequency of the indicated ^1H_N resonance. In the 3D ^{1}H−^{15}N NOESY−HSQC plot (A), intraresidue $d_{N\alpha}$ and $d_{N\beta}$ correlations are boxed. Sequential $d_{N\alpha}(i,i-1)$ and $d_{N\beta}(i,i-1)$ correlations are indicated by arrows beginning at the boxed intraresidue correlation in the preceding slice. Horizontal lines identify sequential $d_{NN}(i,i+1)$ NOEs. In the 3D ^{1}H−^{15}N HSQC−NOESY−HSQC plot (B), the one-bond ^{1}H−^{15}N correlation for each residue is boxed. Sequential d_{NN} correlations are indicated by arrows beginning at the boxed ^{1}H−^{15}N correlation in the preceding slice.

The resulting $J(\omega)$ values and their corresponding standard deviations are plotted in Figure 4 versus the protein sequence. $J(0)$ is simply the average value $J_{avg}(0)$ which equals $^1/_2[J^{400}(0) + J^{600}(0)]$, with the exception of Asp-76 which was measured at 600 MHz only. Taking the average of $J(0)$ values from the two different fields has been justified to average the experimental measurement errors (*12*). From here on, we refer to $J_{avg}(0)$, $J(40)$, and $J(60)$ values as the low-frequency values of $J(\omega)$. $J(360)$ and $J(540)$ are the high-frequency values of $J(\omega)$. These values define for each residue a spectral density function which can be a single Lorentzian or a sum of Lorentzians in the more general case. In Figure 4, the $J(0)$ values are the greatest values in the range of about 2.09−2.90 ns/rad, with an average of 2.63 ± 0.16 ns/rad suggesting that the overall correlation time $\tau_c >$ 6.6 ns. $J(\omega)$ decreases sharply with ω, and average values

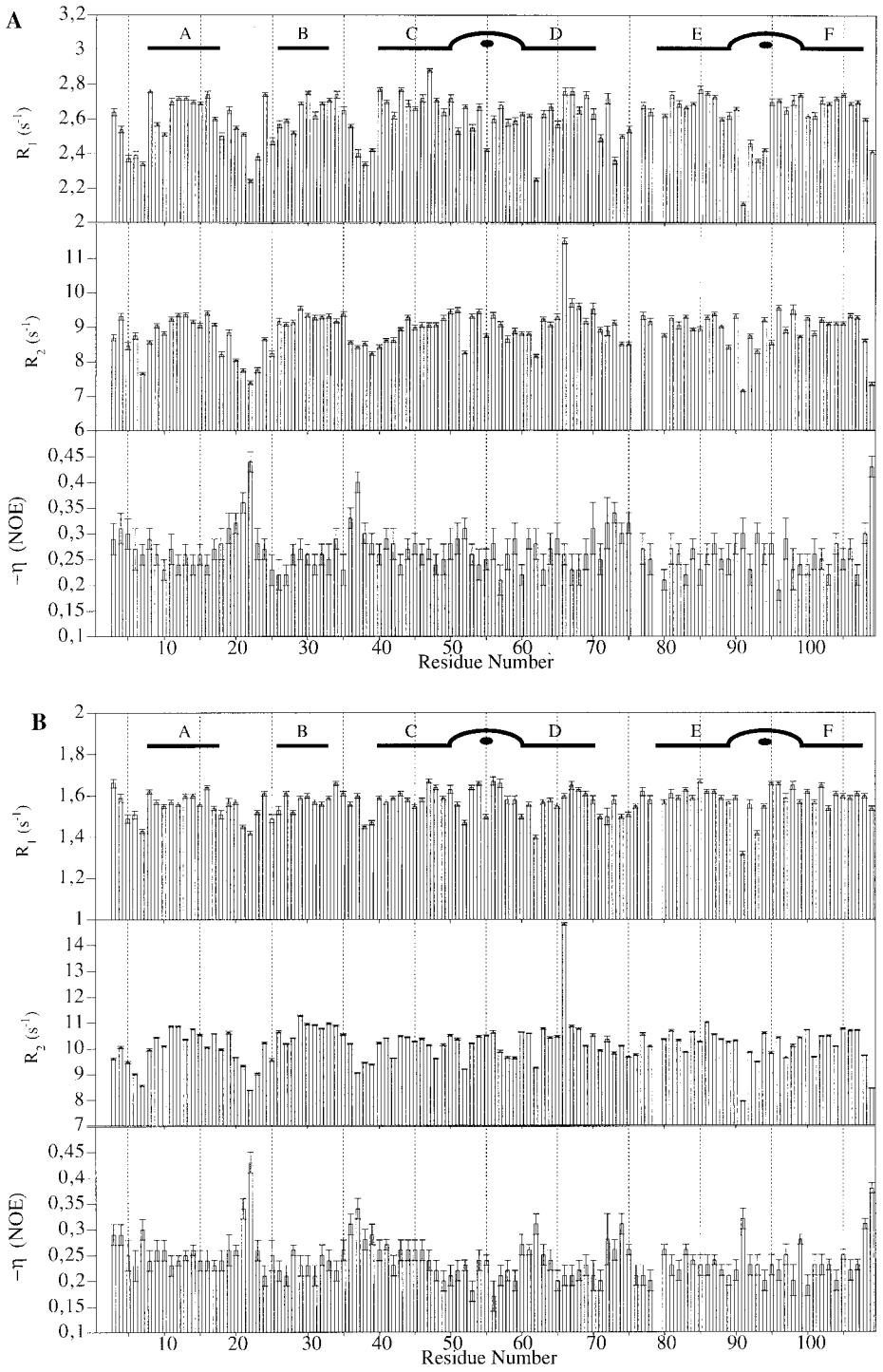

FIGURE 3: Plots of R_1, R_2, and $^1H-^{15}N$ NOE values of Ca^{2+}-loaded rat α-parvalbumin as a function of residue number. Panels A and B refer to data measured at 400 (9.40 T) and 600 MHz (14.10 T), respectively. Standard errors are given by the small bars.

of $J(40)$ and $J(360)$ are 0.564 ± 0.031 and 0.295 ± 0.014 ns/rad, respectively. The $J(360)$ values vary between 0.008 and 0.016 ns/rad with an average of 0.011 ± 0.001 ns/rad. The $J(540)$ values are smaller and vary in the range of 0.0045−0.0094 ns/rad, with an average of 0.0060 ± 0.0008 ns/rad. The $J_{avg}(0)$ profile presents the largest variability within the protein sequence and is apparently the most sensitive probe for the dynamic heterogeneity along the backbone of the rat α-parvalbumin−Ca^{2+}.

Since the area under the spectral density function $J(\omega)$ associated with each NH vector is constant, interdependence between low- and high-frequency values of the spectral density functions is expected and can be used to interpret motions occurring in the Ca^{2+}-loaded rat α-parvalbumin at the five frequencies shown in Figure 4. Therefore, a decrease of the $J(0)$ value is balanced by an increase of the values of $J(\omega)$ at high frequency. This is clearly observed for residues Asp-22 and Lys-37 present in the AB and BC loops, respectively, as well as for the C-terminal residue Ser-109. By contrast, weak contributions of $J(\omega)$ at high frequencies for all six helices and loops CD and EF suggest that these residues are located in very well ordered and rigid domains. Interestingly, values for the low-frequency components of the spectral density function [i.e., $J_{avg}(0)$, $J(40)$, and $J(60)$]

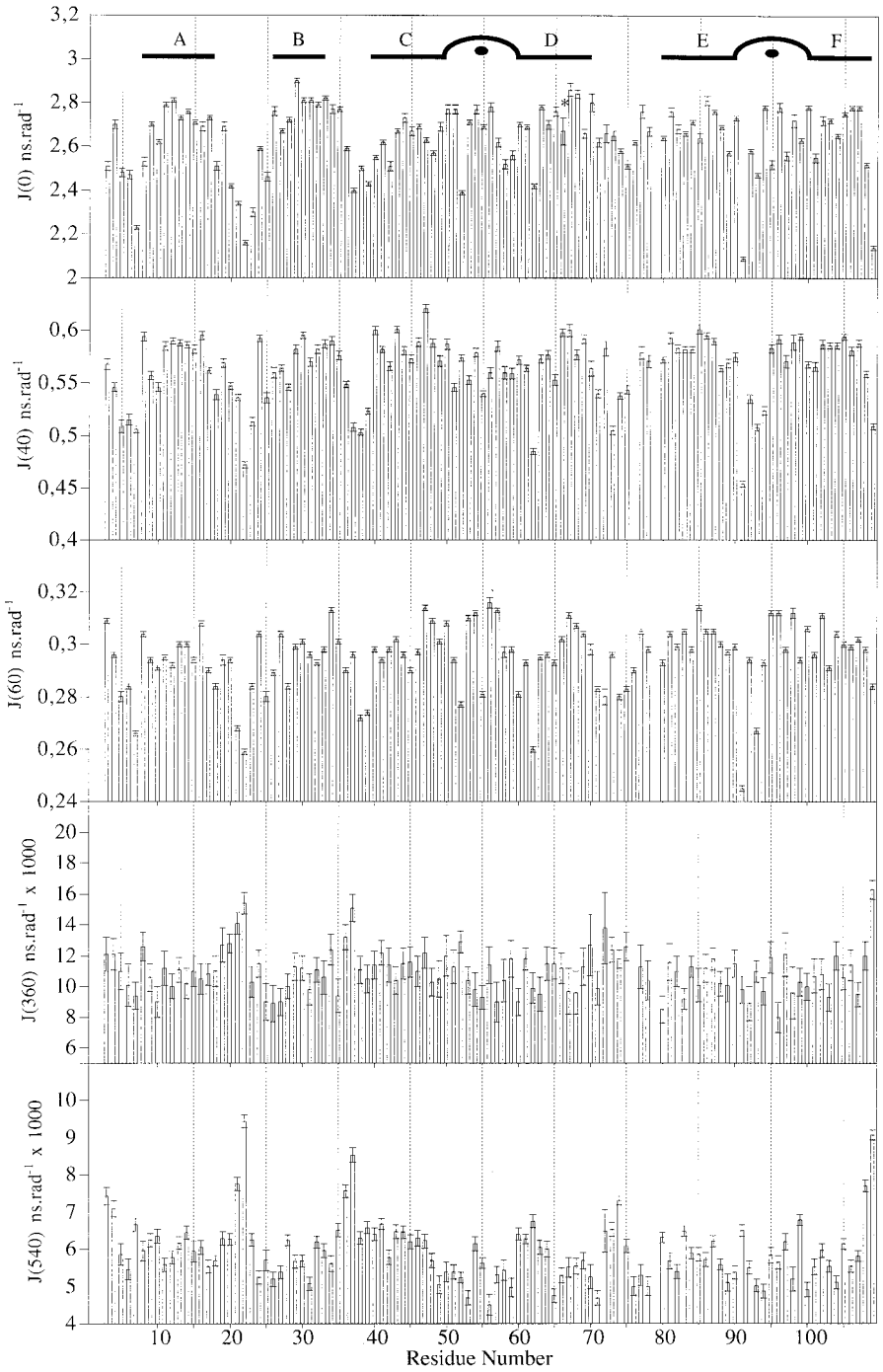

FIGURE 4: Values of the spectral density function $J(\omega)$ vs the protein sequence for Ca^{2+}-loaded rat α-parvalbumin at frequencies of 0, 40, 60, 360, and 540 MHz. Following the work of Ishima and Nagayama (*38*), we used $J^*(\omega_H) = J(\omega_H + \omega_N)$. $J_{avg}(0)$ is averaged over the two field strengths. The value of $J(0)$ for residue Ile-66 (marked with an asterisk) is obtained without contributions of motions on the microsecond to millisecond time scale.

for Lys-52, Glu-62, Lys-91, and Gly-93 exhibit a sharp decrease but without the increase of high-frequency values. This may indicate the presence of fast motions on a time scale much shorter than the overall molecular tumbling (i.e., possibly faster than the picosecond time scale). The increase of high-frequency contributions of $J(\omega)$ for these residues would probably be achieved at higher frequencies than the observable range (*38*).

Lipari-Szabo model-free analysis

Overall Rotational Correlation Time τ_m. The shape of the rat parvalbumin molecule is approximately spherical with an average tensor ratio $D_{||}/D_{\perp}$ of 1.16, and therefore, we have assumed an isotropic overall motion of the protein. The value of τ_m was determined to be 7.6 ns according to the R_2/R_1 ratio (see Materials and Methods). This value is comparable to those reported for small proteins (*2*−*5*, *7*−*11*, *14*). In the case of Ca^{2+}-loaded pike parvalbumin, a value of 8 ns was determined from ^{13}C relaxation data at natural abundance at a concentration of 13 mM (*29*).

Model-Free Analysis. The model-free analysis has the advantage of removing contributions from the overall correlation time and thus allows the comparison of dynamical results obtained for various proteins. The relaxation param-

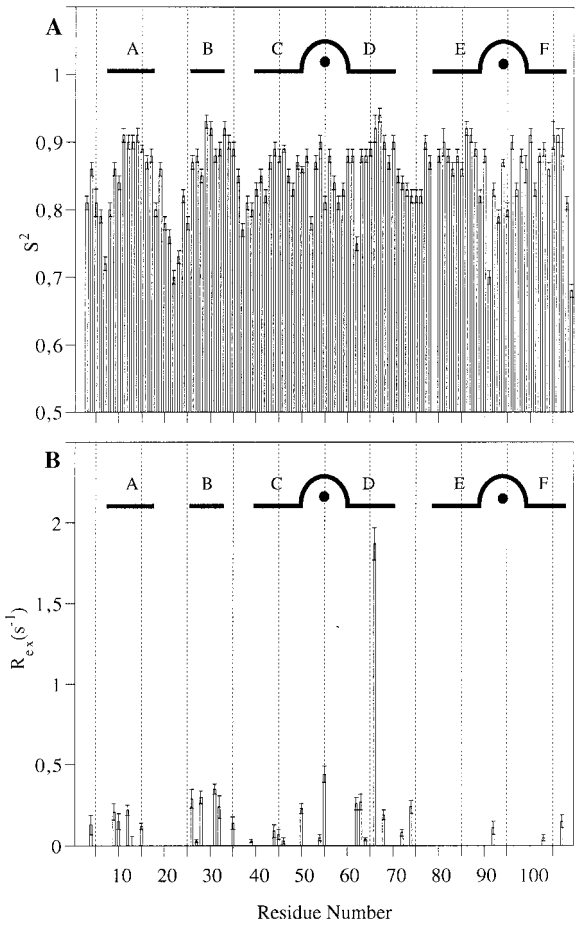

FIGURE 5: Plots of the generalized order parameters S^2 (A) and line width exchange parameters $R_{ex,ls}^{400}$ (B) as a function of residue number for Ca^{2+}-loaded rat α-parvalbumin are shown. These values are based on both data sets recorded at 9.40 (400 MHz) and 14.10 T (600 MHz).

eters of each residue at both spectrometer frequencies (i.e., 400 and 600 MHz) were fitted using the different spectral density function models I−V, as given in Table 2. The optimum spectral density models were selected as described above according to Farrow et al. (*46*). Relaxation data were fitted with model II (S^2 and τ_e) for 12 residues, with model III (S_f^2, S_s^2, and τ_e) for 65 residues, and with model V (S^2 and R_{ex}) for 29 residues (Supporting Information).

The S^2 value measures the amplitude of the internal motion contributing to relaxation. The average value of the order parameter S^2 over all residues is 0.85 ± 0.05. Again, several NH bond vectors of the protein appear to be more mobile on the picosecond to nanosecond time scale than the average as shown in Figure 5A. They include Leu-6 and Ser-7 at the N terminus, Ala-20, Asp-22, and Ser-23 in loop AB, Lys-37 in loop BC, and Glu-108 and Ser-109 at the C terminus. Single low S^2 values are also observed for Lys-52, Ser-55, Glu-62, and Lys-91.

Conformational Exchange Parameter R_{ex}. The residues requiring a non-zero $R_{ex,ls}$ parameter in the Lipari−Szabo formalism (ls subscript) are shown in Figure 5B. Small $R_{ex,ls}$ values are required for some residues in helices A and B, and the Ca^{2+} binding domain CD (values smaller than 0.5 s^{-1}). Again, a large R_{ex}^{400} is observed for residue Ile-66 (1.87 ± 0.1 s^{-1}), not differing greatly from the one previously determined from spectral density mapping. It is interesting to note that Ile-66 belongs to helix D which is characterized in all known parvalbumin structures by a tightly bent conformation. The break occurs at the level of Ser-65, which departs from the helical Φ and Ψ angles combination.

DISCUSSION

The analysis of ^{15}N relaxation data using spectral density mapping at two frequencies and the Lipari−Szabo formalism indicates that the Ca^{2+}-loaded form of the rat α-parvalbumin is remarkably rigid. The deviations from the average S^2 (i.e., 0.85) are small and do not exceed 0.15. This corresponds to a small amplitude of the internal motion of the amide NH vectors on the picosecond to nanosecond time scale. Typically, continuous variations are observed for the AB loop and for the BC loop which links the AB domain (or AB flap) to the more compact CD and EF domains as well as for the N- and C-terminal regions. Four single amide NH vectors of residues Lys-52, Glu-62, Lys-91, and Gly-93, located in the CD and EF domains, display steep variations corresponding to very fast motions with large amplitudes. It is interesting to note that Lys-52 and Lys-91 belong to the Ca^{2+}-binding loops where they occupy the same relative position, 2.

The local mobility of the $^{15}N-H$ amide vector is mainly defined at the level of the $CO_{i-1}-NH_i$ peptide plane. Hydrogen bonds to this peptide plane and hydrophobic interactions involving neighboring side chains are therefore expected to reduce the plane's mobility, and therefore that of the NH_i vector. The presence of three molecules in the same crystal unit cell (*28*) gives us an opportunity to analyze the variability of the peptide plane conformations between three structures for all $CO_{i-1}-NH_i$ peptide bonds through correlated variations of the close torsion angles $\Delta\Psi_{i-1}$ and $\Delta\Phi_i$, also called "crankshaft motions" (*51*). The product of the differences $\Delta\Psi_{i-1} \times \Delta\Phi_i$ in the three molecules is used to represent the variability of each peptide plane *i*. The largest values are observed for residues Met-2, Phe-18, Lys-38, Ser-55, Glu-62, Lys-91, and Ser-109, indicating a large variation in the orientation of their peptide planes. Indeed, low S^2 values are observed for these residues. However, low S^2 values are observed for Ser-7, Asp-22, and Lys-37, while the orientation of the peptide plane is almost conserved. The absence of any detectable change in the orientation of these peptide planes between the three molecules in the crystal structure might be related to crystal packing effects. The analysis of the H-bond network also indicates that the $CO_{i-1}-NH_i$ peptide planes involving residues *i* of Ser-7, Ala-20, Lys-37, Lys-38, and Ser-39 do not display hydrogen bonding. The absence of stabilizing hydrogen bonds at the backbone level for these residues probably contributes to their relative mobility (i.e., low S^2 values).

N and C Termini. In rat α-parvalbumin, the NH vectors at the N- and C-terminal ends display S^2 values higher than those observed for similar residues in many other proteins (*3*, *8*, *12*, *30*, *46*, *52*−*56*). The lowest S^2 value (0.68) is observed for Ser-109. At the N terminus, hydrogen bonds and hydrophobic contacts are found that anchor residues within a small α-helix (spanning Ser-1 to Leu-6) to residues of the B and D helices and the BC loop (*28*). At the C terminus, the carboxylate group of the residue Ser-109 interacts with Gln-31 $N^{\epsilon 2}$ (helix B) and Lys-36 N^{ζ} (BC loop).

These contacts are expected to reduce the mobility of the C terminus of helix F and serve to fix the last residues to the rest of the protein core. This feature is absent in other EF-hand proteins as well as in parvalbumins of the β-lineage. In the case of pike parvalbumin, the $H_\alpha C$ vectors display the lowest S^2 values (0.48 and 0.5) for N- and C-terminal residues (*29*), respectively.

AB Domain. The mobility of the AB loop as shown in Figures 4 and 5 remains relatively small compared with those of loops in other proteins. A minimum S^2 value of 0.70 is progressively obtained for the NH vector of residue Asp-22, but residues Thr-19 and Phe-24 in the loop display a reduced mobility similar to residues present in the helices. The relatively weak amplitude of internal motions of the NH vectors of residues in this loop arises from several structural features that involve Phe-18, Asp-22, Phe-24, and the salt bridge between Arg-75 and Glu-81 (*28*). The NHs of Asp-22 and Phe-24 are hydrogen bonded to the Glu-81 carboxylate group. The carbonyl of the Phe-18 is within hydrogen bond distance of both N^ϵ and N^η atoms of the Arg-75 side chain. This is consistent with the HN^ϵ of Arg-75 which displays a relatively weak mobility ($S^2 = 0.63$). Such a network of hydrogen bonds probably represents the main contribution that reduces the mobility of the NH vectors of the AB loop. This relative rigidity must be reinforced by the interaction of the Phe-24 side chain with the hydrophobic core of the protein.

CD and EF Domains. The dynamical properties of the CD and EF domains clearly differ from those of the AB domain as shown in Figures 4 and 5. Both Ca^{2+}-binding loops are relatively rigid with $\langle S^2 \rangle$ values of 0.85 for the CD site and of 0.82 for the EF site. The flanking helices are more rigid with $\langle S^2 \rangle$ values of 0.85 (helix C), 0.87 (helix D), and 0.88 (helices E and F). Although they present a conserved structural arrangement (*57*) with an approximate 2-fold symmetry axis (*18*), the dynamic properties of the two Ca^{2+}-binding sites are not strictly identical as far as they can be compared in Figures 4 and 5. The low S^2 values observed for residues 52 and 91 are interesting as they pertain to residues occupying symmetrical positions at the beginning of both Ca^{2+}-binding loops. These two residues, 52 and 91, are involved in two symmetrical γ-turns 50−52 and 89−91 (*28*, *57*) which both constitute a flexible hinge between two rigid structures, namely, the incoming helix, C or E, and the Ca^{2+}-binding loop, CD or EF, respectively. The increase in mobility observed for residue 62 in the exiting helix D can be related to the mobility of the corresponding amide plan in the X-ray structure as reported above. A similar mobility is not observed for symmetrical residue 101 in helix F. This must be related to the distortion of helix D in comparison to the more regular helix F.

Conformational Exchange at Residue Ile-66. The bending of helix D corresponds to a break of regularity in the H-bond pattern in this helix. The chemical exchange observed for residue 66 indicates that not only the structure but also dynamical processes must be involved in the bending of helix D. The analysis of ^{15}N relaxation data is not only restricted to motions on a fast time scale (picosecond to nanosecond), but it also provides information through R_{ex} terms on processes occurring on a slower time scale (microsecond to millisecond). Direct mapping of the spectral density function $J(\omega)$ and the Lipari-Szabo formalism analysis show a strong contribution of R_{ex} at residue Ile-66. The NH of this residue is involved in, at least, one hydrogen bond with the CO of residue Leu-63. Moreover, this NH is protected from chemical exchange with the solvent, as previously measured from NH exchange rates on pike parvalbumin (*24*) and confirmed by similar studies with rat parvalbumin (unpublished results). Because chemical exchange of the amide proton is excluded, the R_{ex} contribution at residue Ile-66 is probably the result of a conformational exchange. Interestingly, the geometry between the H-bond acceptors, COs of residues Glu-62 and Leu-63, and the NH of Ile-66 is different in the three structures in the crystal (*28*). A H-bond between Ile-66 and Leu-63 is common to all three molecules, but two molecules display a forked H-bond between NH Ile-66, CO Glu-62, and CO Leu-63. Therefore, the conformational exchange observed at residue Ile-66 could represent variations of the geometry of these hydrogen bonds seen on the microsecond to millisecond time scale. This conformational change could be simply due to local variation in the environment of the amide nitrogen of Ile-66 because of a change in the pattern of H-bonding or could be linked to fluctuations of the α-helix and 3^{10}-helix segments of helix D relative to each other. Interestingly, in the ^{13}C relaxation study of pike parvalbumin, R_{ex} contributions within helix D are negligible. Thus, the conformational exchange observed with ^{15}N relaxation for rat parvalbumin at residue Ile-66 involves hydrogen bonds specifically. This argument is supported by the high structural conservation of the α-parvalbumin fold.

^{15}N and ^{13}C Relaxation. The availability of dynamic information about $C_\alpha H$ vectors of the pike parvalbumin−Ca^{2+} allows a comparison with the behavior of NH vectors of the rat parvalbumin determined in this study. The two parvalbumins from rat and pike as studied respectively by ^{15}N and ^{13}C relaxation differ by 43 mutations over 109 residues, so a strict comparison cannot be performed. However, the average S^2 value for $^{13}C_\alpha H$ is 0.84 and S^2 value for ^{15}NH is 0.85, suggesting the overall rigidity of α-parvalbumins. The S^2 profiles of NH and $C_\alpha H$ vectors are rather different and do not show any evident correlations. One of the differences occurs at the level of the AB loop, where the NH vectors are relatively more mobile than the $C_\alpha H$ vectors. Indeed, there is a significant difference in S^2 between the NH and $C_\alpha H$ vectors for residues 20 and 23. This difference in behavior between NH and $C_\alpha H$ vectors for these residues possibly mirrors a dissociated mobility between the $C_\alpha H$ vectors and the peptide plane (NH and CO vectors). This is expected since the mobilities of the $C_\alpha H$ vectors are mainly affected by side chain constraints (hydrophobic or ionic interactions), whereas the dynamics of peptide planes are rather affected by hydrogen bonds. From this point of view, only the motions of NH and CO vectors are really correlated (*58*, *59*). A strict comparison between HN and $C_\alpha H$ vector dynamics would require studies on the same parvalbumin (either rat or pike).

Comparison with Other EF-Hand Pairs. The availability of ^{15}N relaxation data for other members of the EF-hand Ca^{2+}-binding protein superfamily prompted us to compare the dynamics of the EF-hand domains which are phylogenetically related (*60*). This present comparison includes the C-terminal domain of Ca^{2+}-loaded calmodulin (*30*), the Ca^{2+}-

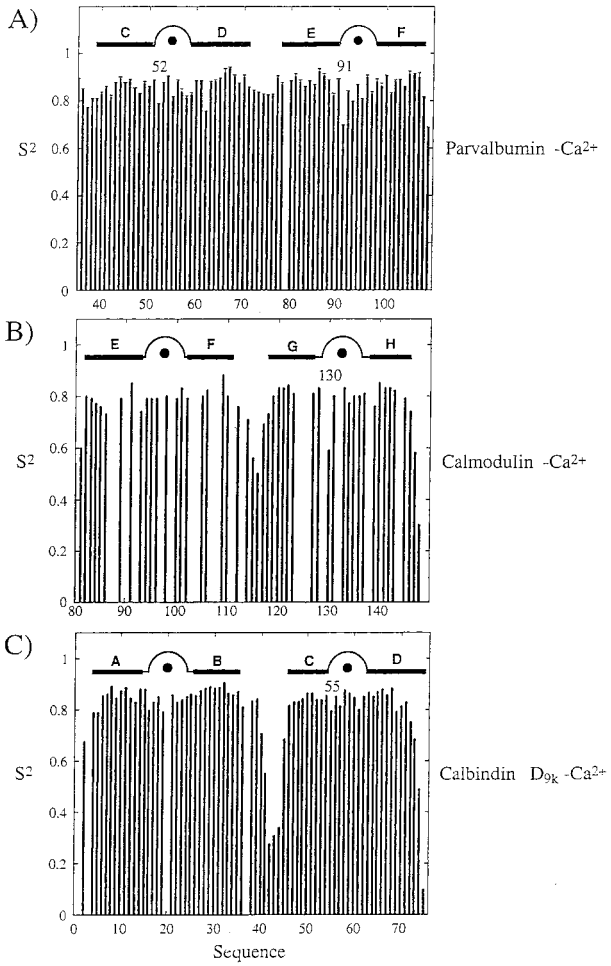

FIGURE 6: Comparison of S^2 order parameters of (A) parvalbumin−Ca^{2+}, (B) the C-terminal domain of calmodulin−Ca^{2+} (*30*), and (C) calbindin D_{9k}−Ca^{2+} (*6*).

loaded calbindin D_{9k} (*6*, *53*), and the Ca^{2+}-loaded rat parvalbumin (this work). Figure 6 compares through their S^2 patterns the C-terminal EF-hand pairs in these proteins. It readily establishes that EF-hand motifs must be considered rigid domains including both helices (the average S^2 value for the three proteins is 0.84) and the Ca^{2+}-binding loop (the average S^2 value for the three proteins is 0.82). There is a tendency toward high mobility (i.e., low S^2 value) for the NH vector of the residue at position 2 in the Ca^{2+}-binding loop. In rat parvalbumin−Ca^{2+}, residue Lys-91 (relative position 2) displays an S^2 value of 0.70 and the corresponding residue in the C-terminal domain of calmodulin−Ca^{2+} (Ile-130, relative position 2) displays an S^2 value of 0.63. In the N-terminal domain of the calmodulin−Ca^{2+} (*30*), the residue at relative position 2 (Ala-57) displays an S^2 value of 0.69. In calbindin−Ca^{2+}, a similar high mobility in relative position 2 is not observed for Lys-55 with an S^2 value of 0.79 (see Figure 6). The remarkable high mobility at position 2 of the calcium binding loop in calmodulin and parvalbumin is mainly observed for the second EF hand of the EF-hand pair and corresponds to a break of S^2 values compared to neighboring residues. This feature differs from what is usually observed in loops where the S^2 profile progressively decreases from the edges to the center of the loop. The fast dynamics at relative position 2 in the Ca^{2+}-binding loops is tentatively attributed to a mobile junction between two rigid motifs: the incoming helix and the Ca^{2+}-binding loop.

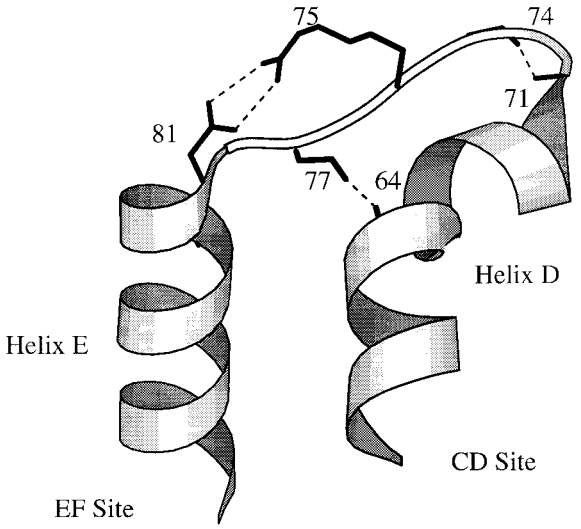

FIGURE 7: Structural elements involving residues of the loop between D and E helices in rat α-parvalbumin−Ca^{2+} (*28*). A conserved salt bridge between Arg-75 and Glu-81 and hydrogen bonds between Gly-64 CO and Leu-77 NH and between Ser-71 CO and Ala-74 NH.

A main difference in the dynamics between these three proteins (i.e., C-terminal domain of calmodulin−Ca^{2+}, calbindin−Ca^{2+}, and parvalbumin−Ca^{2+}) occurs at the level of the linker connecting EF-hand pairs. The highest linker mobility is observed in calbindin D_{9k} (residues 36−45) with an S^2 value of 0.28 at residue Gly-42. Similarly, the linker in the C-terminal domain of calmodulin (residues 113−117) presents an important mobility at residue Leu-116 with an S^2 value of 0.50. On the contrary, the parvalbumin linker (residues 71−78) does not correspond to a flexible loop, where the maximum mobility is observed at residue Ala-74 with an S^2 of 0.82. As shown in Figure 7, the parvalbumin linker has an extended conformation running along the last half of helix D, with hydrogen bonds between CO of Gly-64 and NH Leu-77, in the turn region between CO Ser-71 and NH Ala-74, and in the Asx turn between Ser-71 and Asp-73 (*28*). The salt bridge between Arg-75 and Glu-81 serves to further stabilize this linker region in parvalbumin. The main parts of the linkers of the C-terminal domain of calmodulin or calbindin are not stabilized by such salt bridges or hydrogen bonds and consequently are very flexible segments.

Another difference between parvalbumin−Ca^{2+}, calmodulin−Ca^{2+}, and calbindin−Ca^{2+} occurs in the C-terminal region. Indeed, Ser-109, the last residue at the C terminus of parvalbumin−Ca^{2+}, is remarkably immobile (i.e., S^2 = 0.68) compared to similar regions in the other calcium-binding proteins. The carboxylate group of the last residue in parvalbumin is firmly docked to the BC loop and B helix through a network of hydrogen bonds and electrostatic interactions. In calbindin−Ca^{2+} (last residue is Gln-75, S^2 = 0.10) or calmodulin−Ca^{2+} (last residue is Lys-148, S^2 = 0.30), the C terminus is not in contact with other parts of the protein and appears to be more mobile. The absence of C-terminal residue 109 in parvalbumins of the β-lineage relative to that of parvalbumins of the α-lineage and the knowledge of X-ray structures of parvalbumins from both lineages led us to expect an increased mobility for the C-terminal region of β-parvalbumins which presumably also present a lower thermal stability (*21*).

We also compared slow motions and/or NH exchange contributions on the microsecond to millisecond time scale using R_{ex} terms between calbindin−Ca^{2+}, calmodulin−Ca^{2+}, and parvalbumin−Ca^{2+}. No common behavior of R_{ex} appears to be conserved within these proteins, probably because R_{ex} terms represent different phenomena. Calbindin−Ca^{2+} has no detectable R_{ex} terms, while parvalbumin−Ca^{2+} has a strong R_{ex} contribution at Ile-66 which is related to the break of helix D. In calmodulin−Ca^{2+}, several R_{ex} terms are found spread over the four EF hands.

CONCLUSION

Part of the specific dynamics in parvalbumin−Ca^{2+} appears to be strongly dependent on the three-dimensional arrangement around the strictly conserved Glu-81−Arg-75 salt bridge. These key residues are involved in several interactions resulting in a reduced mobility of the DE segment which further locks the CD and EF domains together. Furthermore, the interaction between the AB loop and the salt bridge and hydrophobic contacts involving the A, B, and D helices are known to play an important role in the affinity for Ca^{2+} ions (*61*). Thus, it is not surprising that no obvious correlation exists between the increase in mobility of the linkers from parvalbumin, calmodulin, and calbindin and their respective affinities for Ca^{2+}. Parvalbumin is probably the most rigid of the EF-hand proteins. The EF-hand motifs (helix−loop−helix) have a conserved low mobility when Ca^{2+} is bound. In the calcium-binding loop, relative position 2 exhibits an increased mobility (in parvalbumin and calmodulin) which represents a flexible hinge between two rather rigid elements, the incoming helix E and the forthcoming Ca^{2+}-binding loop. The rigidity of the DE segment and C terminus in parvalbumin enhances helix stability and probably anchors the ends of the coordinating loops (*62*, *63*) in a proper geometry for calcium binding. To address the question of whether this rigidity is conserved without the AB domain and how this affects the structure of the rest of the protein, we have commenced a study of the truncated parvalbumin lacking this domain (work in progress).

ACKNOWLEDGMENT

We are indebted to Drs. Jean-François Lefèvre, Joël Mispelter, and Jean-Marc Lhoste for helpful discussion during the course of these studies. We thank Dr. Paul Bello for correcting the grammar. La Direction de la Coopération Scientifique et Technique du Ministère des Affaires Etrangères et l'Ambassade de France en Suisse are greatly acknowledged for their help in this project.

SUPPORTING INFORMATION AVAILABLE

A table of chemical shifts of ^{15}N and ^{1}H amide resonances and two tables of R_1, R_2, η, and S^2 values (7 pages). Ordering information is given on any current masthead page.

REFERENCES

1. Williams, R. J. P. (1989) *Eur. J. Biochem. 183*, 479−497.
2. Kay, L. E., Torchia, D. A., and Bax, A. (1989) *Biochemistry 28*, 8972−8979.
3. Clore, G. M., Driscoll, P. C., Wingfield, P. T., and Gronenborn, A. M. (1990) *Biochemistry 29*, 7387−7401.
4. Redfield, C., Boyd, J., Smith, L. J., Smith, R. A. G., and Dobson, C. M. (1992) *Biochemistry 31*, 10431−10437.
5. Powers, R., Clore, G. M., Stahl, S. J., Wingfield, P. T., and Gronenborn, A. M. (1992) *Biochemistry 31*, 9150−9157.
6. Kördel, J., Skelton, N. J., Akke, M., Palmer, A. G., III, and Chazin, W. J. (1992) *Biochemistry 31*, 4856−4866.
7. Berglund, H., Kovàcs, H., Dahlman-Wright, K., Gustafsson, J., and Härd, T. (1992) *Biochemistry 31*, 12001−12011.
8. Stone, M. J., Chandrasekhar, K., Holmgren, A., Wright, P. E., and Dyson, H. J. (1993) *Biochemistry 32*, 426−435.
9. Cheng, J. W., Lepre, C. A., Chambers, S. P., Fulghum, J. R., Thomson, J. A., and Moore, J. M. (1993) *Biochemistry 32*, 9000−9010.
10. Fushman, D., Weisemann, R., Thüring, H., and Rüterjans, H. (1994) *J. Biol. Nucl. Magn. Reson. 4*, 61−78.
11. Yamasaki, K., Saito, M., Oobatake, M., and Kanaya, S. (1995) *Biochemistry 34*, 6587−6601.
12. Peng, J. W., and Wagner, G. (1995) *Biochemistry 34*, 16733−16752.
13. Farrow, N. A., Zhang, O., Szabo, A., Torchia, D. A., and Kay, L. E. (1995) *J. Biomol. Nucl. Magn. Reson. 6*, 153−162.
14. Nicholson, L. K., Yamasaki, T., Torchia, D. A., Grzesiek, S., Bax, A., Stahl, S. J., Kaufman, J. D., Winfield, P. T., Lam, P. Y. S., Jadhav, P. K., Hodge, N., Domaille, P. J., and Chang, C. H. (1995) *Nat. Struct. Biol. 2*, 274−280.
15. Kretsinger, R. H. (1980) *CRC Crit. Rev. Biochem. 8* (2), 119−174.
16. Persechini, A., Moncrief, N. D., and Kretsinger, R. H. (1989) *Trends Neurosci. 12* (11), 462−467.
17. Kawasaki, I., and Kretsinger, R. H. (1994) *Protein Profile 1*, 343−391.
18. Kretsinger, R. H., and Nockolds, C. E. (1973) *J. Biol. Chem. 248*, 3313−3326.
19. Vogel, H. J. (1994) *Biochem. Cell. Biol. 72*, 357−376.
20. Chard, P. S., Bleakman, D., Christakos, S., Fullmer, C. S., and Miller, R. J. (1993) *J. Physiol. 472*, 341−357.
21. Williams, T. C., Corson, D. C., Oikawa, K., McCubbin, W., Kay, C. M., and Sykes, B. D. (1986) *Biochemistry 25*, 1835−1846.
22. Padilla, A., Cavé, A., and Parello, J. (1988) *J. Mol. Biol. 204*, 995−1017.
23. Padilla, A., Vuister, G. W., Boelens, R., Kleyvegt, G. J., Cavé, A., Parello, J., and Kaptein, R. (1990) *J. Am. Chem. Soc. 112*, 5024−5030.
24. Baldellon, C., Padilla, A., and Cavé A. (1992) *Biochimie 74*, 837−844.
25. Roquet, F., Declercq, J. P., Tinant, B., Rambaud, J., and Parello, J. (1992) *J. Mol. Biol. 223*, 705−720.
26. Declercq, J. P., Tinant, B., Parello, J., Etienne, G., and Huber, R. (1988) *J. Mol. Biol. 202*, 349−353.
27. Declercq, J. P., Tinant, B., Parello, J., and Rambaud, J. (1991) *J. Mol. Biol. 220*, 1017−1039.
28. McPhalen, C. A., Sielecki, A. R., Santarsiero, B. D., Swensen, L., and James, M. N. G. (1994) *J. Mol. Biol. 235*, 718−732.
29. Alattia, T., Padilla, A., and Cavé, A. (1996) *Eur. J. Biochem. 237*, 561−574.
30. Barbato, G., Ikura, M., Kay, L. E., Pastor, R. W., and Bax, A. (1992) *Biochemistry 31*, 5269−5278.
31. Pauls, T. L., Durussel, I., Cox, J. A., Clark, I. D., Szabo, A. G., Gagné, S. M., Sykes, B. D., and Berchtold, M. W. (1993) *J. Biol. Chem. 268*, 20897−20903.
32. Sambrook, J., Fritsch, E. F., and Maniatis, T. (1989) in *Molecular cloning: a laboratory manual*, Cold Spring Harbor Laboratory Press, Plainview, NY.
33. Peng, J. W., and Wagner, G. (1992) *J. Magn. Reson. 98*, 308−332.
34. Neidig, K. P., Geyer, M., Göler, A., Antz, C., Saffrich, R., Beneicke, W., and Kalbitzer, H. R. (1995) *J. Biomol. Nucl. Magn. Reson. 6*, 255−270.
35. Palmer, A. G., III, Rance, M., and Wright, P. E. (1991) *J. Am. Chem. Soc. 113*, 4371−4379.
36. Press, W. H., Flannery, B. P., Teutolski, S. A., and Vetterling, W. T. (1986) in *Numerical recipies*, Cambridge University Press, Cambridge, U.K.

37. Peng, J. W., and Wagner, G. (1992) *Biochemistry 31*, 8571−8586.
38. Ishima, R., and Nagayama, K. (1995) *Biochemistry 34*, 3162−3171.
39. Lefèvre, J. F., Dayies, K. T., and Wagner, G. (1996) *Biochemistry 35*, 2674−2686.
40. Farrow, N. A., Zhang, O., Forman-Kay, J., and Kay, L. E. (1997) *Biochemistry 36*, 2390−2402.
41. Abragam, A. (1961) in *The Principles of Nuclear Magnetism*, Oxford University Press (Clarendon), Oxford, U.K.
42. Ernst, R. R., Bodenhausen, G., and Wokaun, A. (1987) in *Principles of Nuclear Magnetic Resonance in One and Two Dimensions*, Clarendon Press, Oxford, U.K.
43. Lipari, G., and Szabo, A. (1982) *J. Am. Chem. Soc. 104*, 4546−4559.
44. Lipari, G., and Szabo, A. (1982) *J. Am. Chem. Soc. 104*, 4559−4570.
45. Clore, G. M., Szabo, A., Bax, A., Kay, L. E., Driscoll, P. C., and Gronenborn, A. M. (1990) *J. Am. Chem. Soc. 112*, 4989−4991.
46. Farrow, N. A., Muhandiram, R., Singer, A. U., Pascal, S. M., Kay, C. M., Gish, G., Shoelson, S. E., Pawson, T., Forman-Kay, J. D., and Kay, L. E. (1994) *Biochemistry 33*, 5984−6003.
47. Marion, D., Kay, L. E., Sparks, S. W., Torchia, D. A., and Bax, A. (1989) *J. Am. Chem. Soc. 111*, 1515−1517.
48. Gronenborn, A. M., Bax, A., Wingfield, P. T., and Clore, G. M. (1989) *FEBS Lett. 243*, 93−98.
49. Ikura, M., Bax, A., Clore, G. M., and Gronenborn, A. M. (1990) *J. Am. Chem. Soc. 112*, 9020−9022.
50. Frenkiel, T., Bauer, C., Carr, M. D., Birdsall, B., and Feeney, J. (1990) *J. Magn. Reson. 90*, 420−425.
51. Fadel, A. R., Jin, D. Q., Montelione, G. T., and Levy, R. M. (1995) *J. Biomol. Nucl. Magn. Reson. 6*, 221−226.
52. Stone, M. J., Fairbrother, W. J., Palmer, A. G., III, Reizer, J., Saier, M. H., Jr., and Wright, P. E. (1992) *Biochemistry 31*, 4394−4406.
53. Akke, M., Skelton, N. J., Kördel, J., Palmer, A. G., III, and Chazin, W. J. (1993) *Biochemistry 32*, 9832−9844.
54. Schneider, D. M., Dellwo, M. J., and Wand, A. J. (1992) *Biochemistry 31*, 3645−3652.
55. Markus, M. A., and Dayies, K. T. (1996) *Biochemistry 35*, 1722−1732.
56. Mandel, A. M., Akke, M., and Palmer, A. G., III (1995) *J. Mol. Biol. 246*, 144−163.
57. Strydnaka, N. C. J., and James, M. N. G. (1989) *Annu. Rev. Biochem. 58*, 951−998.
58. Dayies, K. T., and Wagner, G. (1995) *J. Magn. Reson. 109*, 105−108.
59. Engelke, J., and Rüterjans, H. (1997) *J. Biomol. Nucl. Magn. Reson. 9*, 63−78.
60. Heizmann, S. R., and Hunziker, W. (1991) *Trends Biochem. Sci. 16*, 98−103.
61. Permyakov, E. A., Medvedkin, V. N., Mitin, Y. V., and Kretsinger, R. H. (1991) *Biochim. Biophys. Acta 1076*, 67−70.
62. Marsden, B. J., Hodges, R. S., and Sykes, B. D. (1989) *Biochemistry 28*, 8839−8847.
63. Trigo-Gonzalez, G., Awang, G., Racher, K., Neden, K., and Borgford, T. (1993) *Biochemistry 32*, 9826−9831.
64. Bodenhausen, G., and Ruben, D. L. (1980) *Chem. Phys. Lett. 69*, 185−188.
65. John, B. K., Plant, D., and Hurd, R. E. (1992) *J. Magn. Reson., Ser. A 101*, 113−117.
66. Wider, G., and Wüthrich, K. (1993) *J. Magn. Reson., Ser. B 102*, 239−241.
67. Bax, A., and Pochapsky, S. S. (1992) *J. Magn. Reson. 99*, 638−643.
68. Van Doren, S. R., Kurochkin, A. V., Ye, Q. Z., Johnson, L. L., Hupe, D. J., and Zuiderweg, E. R. P. (1993) *Biochemistry 32*, 13109−13122.
69. Shaka, A. J., Barher, P. B., and Freeman, R. (1985) *J. Magn. Reson. 64*, 547−552.
70. Carr, H. Y., and Purcell, E. M. (1954) *Phys. Rev. 94*, 630−639.
71. Meiboom, S., and Gill, D. (1958) *Rev. Sci. Instrum. 29*, 688−691.
72. Kay, L. E., Nicholson, L. K., Delaglio, F., Bax, A., and Torchia, D. A. (1992) *J. Magn. Reson. 97*, 359−375.
73. Markley, J. L., Horsley, W. J., and Klein, M. P. (1971) *J. Chem. Phys. 55*, 3604−3605.
74. Kraulis, J. (1991) *J. Appl. Crystallogr. 24*, 946−950.

BI980334P